ChemComm

COMMUNICATION

View Article Online
View Journal | View Issue

Cite this: *Chem. Commun.*, 2024, **60**, 8280

Received 28th May 2024,
Accepted 5th July 2024

DOI: 10.1039/d4cc02581d

rsc.li/chemcomm

Tuning the electronic properties of Zr UiO-66 through defect-functionalised multivariate modulation†

Carmen Rosales-Martínez, [a] Marcelo Assis, *[b] Celia Castillo-Blas *[c] and Isabel Abánades Lázaro *[a]

The multivariate modulation of Metal–Organic Frameworks is presented as a valuable tool to introduce multiple functional units into UiO-66 while increasing its porosity. This manuscript encloses a comprehensive study using *p*-functionalised benzoate $-NO_2$, $-SO_3$ and –SH modulators, rationalizing the defects introduced and their impact on properties.

Modulated self-assembly of metal–organic frameworks (MOFs) has emerged as a valuable tool for modifying their properties.[1,2] Among the consequences of the introduction of modulators–organic ligands with fewer coordination sites than the linker, typically monotopic stands the possibility of defect-functionalization.[3,4] Defect engineering has received significant attention as defects can tune the physical and electronic properties of materials.[5,6] In the same context, increasing the heterogeneity of MOFs through functionalization is also a hot topic with enhancement in diverse applications.[7,8] In this regard, multivariate chemistry provides the opportunity to introduce multiple functional groups, leading to pores with opposite dual properties and characteristics that are not the linear combination of their separate counterparts.[9] Combining these two hot topics through defect-engineering multivariate modulation of MOFs, represented in Fig. 1a, results in defect-functionalized multivariate structures with increased porosity and reactivity.[4,10] However, only a few examples are present in the literature, highlighting the need to further develop this concept.

Herein we present a comprehensive study of the defect multifunctionalisation of UiO-66 with *p*-functionalized benzoate (Benz) derivates with $-SO_3^-$, $-NO_2$ and –SH groups through multivariate modulation (MTVM). The co-incorporation of these groups in relation to the induced defects and their resultant structural, physical and electronic properties are investigated.

The modulators were introduced in a 1 to 1 ratio compared to the linker of the Zr-terephthalate (Zr-BDC) MOF UiO-66 (see ESI† S.2). All the samples were highly crystalline, as identified by powder X-ray diffraction (PXRD) (Fig. 1b). Pawley refinements confirmed phase purity (see ESI† S3.1) and showed that all pristine UiO-66 and MTVM UiO-66 materials refine in the $Fm\bar{3}m$ space group, although a contraction of the unit cell is observed for the MTVM materials. Two small broad diffraction peaks that are not present in the pristine MOF (at *ca.* 4.3 and 5.5 2 2theta degrees), appear for the MTVM MOFs (Fig. 1b and Fig. S1–S6, ESI†), indicating the formation of nanodomains of defective ***reo*** phase.[11]

The incorporation of modulators, as characterised by acid-digested ^{1}H NMR (Fig. S7–S11, ESI†), agreed with the modulator acidity – pK_a SH (4.05) > NO_2 (3.44) > SO_3 (3.75/<1) -for

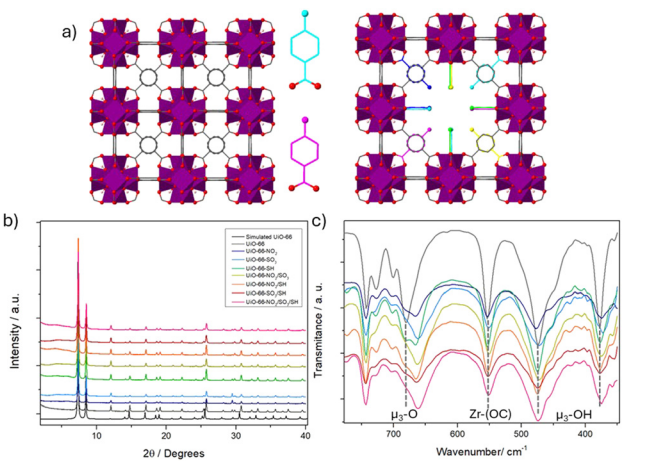

Fig. 1 (a) Schematic representation of MTVM MOF with defect-induced *reo* topology compared with the pristine MOF. (b) PXRD profiles (c) FT-IR profiles highlighting μ_3-O, μ_3-OH and Zr-(OC) bands.

[a] *Instituto de Ciencia Molecular, Universitat de Valencia, Calle catedrático José Beltrán Martínez, 46980, Paterna, Valencia, Spain. E-mail: isabel.abanades@uv.es*
[b] *Biomaterials and Bioengineering Lab, Translational Research Centre San Alberto Magno, Universidad Catolica de Valencia San Vicente Mártir (UCV), Spain*
[c] *Department of Materials Science and Metallurgy, 27 Charles Babbage road, University of Cambridge, CB30FS, Cambridge, UK*

† Electronic supplementary information (ESI) available: Details of synthesis, characterisation, and properties of materials. See DOI: **https://doi.org/10.1039/d4cc02581d**

single-modulated MOFs,[6] with ratios of *ca.* 0.2, 0.07 and 0.04 modulators per linker for UiO-66-SO_3, UiO-66-NO_2 and UiO-66-SH respectively (Table 1), which corresponds to 16.7, 6.7 and 3.9 mol%. The ratio of SO_3/BDC agrees with previous work using this modulator as a hemilabile linker due to the ability of the sulfonate to coordinate with Zr_6 clusters.[12]

In the di-modulated MOFs, different trends in incorporation are observed. For UiO-66-NO_2/SO_3 the presence of Benz-NO_2 in the profiles is almost negligible, whereas Benz-SO_3 is slightly less incorporated than for the single modulated MOF. In UiO-66-NO_2/SH, the Benz-SH modulator (less acidic) is surprisingly more incorporated than the NO_2-derivative modulator, while in UiO-66-SO_3/SH the most acidic modulator, Benz-SO_3, is the most incorporated. Unexpectedly, Benz-SO_3 is the less incorporated in the tri-modulated sample, followed by Benz-SH and Benz-NO_2 derivatives. Interestingly, the unit cell contraction determined by Pawley refinements increases with the modulators incorporated.

The results of the specific synthetic set fully characterized enclosed in this manuscript are given in Table 1, but these trends have been reproduced and expressed as the average and standard deviation in ESI† Section 3.2. The fact that the incorporation trends are not aligned with the modulator's acidity for MTVM MOFs, suggests that repulsion-attraction interactions can have a major role in dictating preferred incorporation.[4] This scenario highlights the complexity, jet beauty of coordination modulation and the need for comprehensive studies with large sets of samples to fully understand it.

FT-IR confirmed the incorporation through coordination, as while vibration bands from the modulators were present, the ones of free carboxylate groups were not observed (Fig. S13–S30, ESI†). In agreement with previous work on Benz-SO_3 modulation, UiO-66-SO_3 displayed shifted bands from Benz-SO_3 coordination.[12] The vibration band that corresponds to μ_3-O stretching (*ca.* 680 cm^{-1})[13] is shifted to *ca.* 660 cm^{-1} upon modulation, with slight variations between samples (Fig. 1c). The band attributed to Zr-(OC) asymmetric stretching[13] has also a minor shift for the samples containing SO_3 groups. This information points out the deformation of the clusters by introducing modulating benzoic acid derivate species.

Thermo Gravimetry Analysis (TGA) revealed high thermal stability (*ca.* 500 °C) upon defect introduction of modulators, with only a significant decrease (to *ca.* 400 °C) for the NO_2-containing samples. The composition of the frameworks was estimated by combining TGA and ^{1}H NMR into mathematical equations (Fig. S31–S36, ESI†).[14] All the samples but UiO-66-SH displayed similar or higher defectivity than the pristine MOF, ranging from 10 to 25 molar% missing linkers (Table 1), with a minimum of 4.5 linkers out of 6 per Zr_6 clusters (9-connected instead of 12-connected units). In the single modulated frameworks, both the number of missing linkers and the incorporation of the modulator agree to its pK_a. Within all the samples, a general but not-so-linear trend of increasing missing linkers (decreasing the linker-to-metal ratio) with the increased incorporation of modulators is observed (Fig. S37, ESI†). UiO-66-SH is the only sample with a slightly lower missing linker percent than pristine UiO-66 (9% *vs.* 11%). This modulator has a pK_a that stands between the pK_{a1} and pK_{a2} of BDC, and a similar log P. In fact, Benz-SH and defect-compensating species (formic acid and acetic acid) fully compensate for the missing linker vacancies, agreeing with recent findings on optimal modulators to boost UiO-66 crystallinity.[15]

X-ray total scattering experiments were conducted to analyze the local structure of the MOFs (Fig. S39–S51, ESI†).[16] The pair distribution function (PDF), denoted as $D(r)$, was used to maximise long-range correlations.[17] Pristine UiO-66 $D(r)$ showed expected correlations similar to the reported UiO-66 ***fcu*** model (Fig. S40–S43, ESI†), including Zr–O (2.2 Å), Zr···Zr (3.5 Å) sharing edges and vertexes and Zr···Zr (4.86 Å) sharing edges within the same cluster. Zr···Zr distances between clusters were also observed in the pristine UiO-66 (Fig. S42, ESI†). MTVM-UiO-66 $D(r)$s exhibited equivalent correlations compared to the pristine MOF, but long-range order peaks had a smaller area due to increased disorder and defects.

More in detail, Zr–O peak centred at 2.2 Å for the pristine UiO-66 is slightly shifted to the left, and a shoulder is also distinguished for the defective samples, as represented in Fig. 2a, suggesting the presence of two different contributions. In addition, Zr–Zr correlations (3.5 Å) of MTVM-derivatives show larger areas, which might indicate a higher number of coordinated Zr, considering the presence of ***reo*** phase according to PXRD patterns. To our knowledge, these facts in PDF patterns have never been reported in Zr-UiO-66 derivatives.

Motivated by the lack of information, total and partial PDFs were recalculated using PDFGUI minimising the ADP values to 0.0005 (Fig. 2b and Fig. S44–S45, ESI†), to extract the contributions from different atom distances.[18] C–H and O–H Contributions are omitted because of their low contribution to the total

Table 1 Characterisation data of the MOFs. Molar ratios compared to the linker (^{1}H NMR), molar missing linker percent (TGA+ ^{1}H NMR), Z-potential, S_{BET} surface area, total pore volume measured at P/P_0 0.9 and estimated optical band gap (eV)

Sample	R NO_2/BDC	R SO_3/BDC	R SH/BDC	ML%	Z-potential	S_{BET}	Pore volume	Band gap
UiO-66	n/a	n/a	n/a	11.0	19.2	1315	0.516	4.21
UiO-66-NO_2	0.072	n/a	n/a	15.2	49.1	1449	0.587	4.07
UiO-66-SO_3	n/a	0.2	n/a	24.9	−5.9	1296	0.546	4.03
UiO-66-SH	n/a	n/a	0.041	9.5	32.2	1339	0.539	3.92
UiO-66-NO_2/SO_3	n/a	0.169	n/a	22.5	14.0	1359	0.548	3.92
UiO-66-NO_2/SH	0.153	n/a	0.186	24.8	31.6	1409	0.563	3.62
UiO-66-SO_3/SH	n/a	0.054	0.015	10.8	22.2	1266	0.52	3.80
UiO-66-NO_2/SO_3/SH	0.169	0.054	0.115	24.5	26.0	1348	0.54	3.67

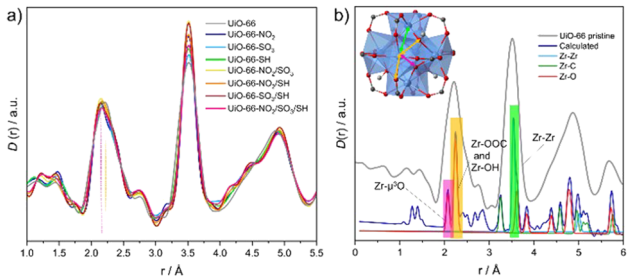

Fig. 2 (a) PDF of the MOFs in the 1.0–5.5 Å range showing peaks centred at 2.2 and 3.5 Å typical from Zr–O and Zr···Zr correlations, respectively. (b) Comparison of the experimental $D(r)$ of the pristine UiO-66 with the calculated partial $g(r)$s using PDFGUI (ADP values are approached to 0.0005). Main correlations are highlighted in pink, yellow and green.

PDF (Fig. S44–S45, ESI†). Peaks centred at 2.07 Å and 2.24 Å correspond to Zr–O-μ_3 and Zr–O_{COO} and Zr–O_{OH}, respectively. Gaussian deconvolution of the pristine UiO-66 peaks centred at 2.2 and 2.78 Å shows a total of 4 peaks (Fig. S46–S47 and Table S10, ESI†). Peak 1 (2.01 Å), and peak 2 (2.21 Å) correspond to the Zr–O-μ_3, Zr–O_{COO} and Zr–O_{OH}, respectively for the pristine sample, whilst peaks 3 and 4 are combined contributions from C···C, C···O and O···O correlations. However, in MTVM-UiO-66 materials, peaks 1–4 shift to the left, suggesting a change in the proportion of the partial correlations or the presence of a different dimensionality of Zr-nodes at the local scale.[19–21] This hypothesis also agrees with an increment of the integrated area of the peak located at 3.5 Å (Table S11 and Fig. S48, ESI†) and shifted peaks located at 4.3, 4.5 and 4.9 Å (Fig. S49–S50, ESI†). PDF patterns for various Zr-node configurations were computed to compare the 2.2 Å peak, indicating shorter correlations with higher atom counts per node (Fig. S51, ESI†). However, further analysis must be carried out to obtain a potential model.

The particle size and morphology were analysed by scanning electron microscopy (SEM) (Fig. S53 and Fig. S52–S55, ESI†). The pristine sample is composed of monodisperse octahedral particles of 296 ± 10 nm. All the samples that do not contain the Benz-SO_3 modulator have also octahedral morphology, and a decrease in particle size, suggesting a capping effect, although the modulator/linker ratio rules out solely incorporation at the particles' surface.[22] Upon the addition of the Benz-SO_3 modulator, the samples are composed of intergrown particles and hollow superstructures of *ca.* 1–3 μm, formed out of nanoparticles of *ca.* 50–100 nm. The reason why these superstructures are formed escapes the understanding of this communication and shall require further study, but we postulate that surface-bond sulfonate groups could be involved. Energy dispersed X-ray Analysis (EDX) (Fig. S56, ESI†) mapping confirmed the homogeneous distribution of S-containing modulators within the structure. The presence of K or Na ions compensating for the charge of unbound SO_3 modulators was discarded by EDX, which showed S/Zr ratios higher than expected for the estimated structure, pointing out the modulators' partial surface incorporation, although this could be affected by interference leading to overestimated S determination and shall be interpreted with caution (Fig. S57, ESI†).

Surface charge is related to defectivity among other factors.[23] All the samples display positive Z-potentials (Table 1), apart from UiO-66-SO_3, whose negative Z-potential suggests the presence of partial tangling sulfonate groups. The rest of the samples (apart from UiO-66-NO_2/SO_3) have an increase in Z-potential, which is not solely related to their defective nature (Fig. S58–S68, ESI†).

N_2 adsorption and desorption isotherms were recorded to evaluate the effect of defect multifunctionalisation on the materials (Fig. S78–S81, ESI†). All the samples displayed higher porosity than expected for pristine UiO-66 (*ca.* 1220 m^2 g^{-1} S_{BET} and 0.40 cm^3 g^{-1} pore volume).[6] Despite introducing significant functionality, the lowest surface area was *ca.* 1266 m^2 g^{-1} for UiO-66-SO_3/SH, which displayed a similar linker-to-metal ratio to the pristine sample. A general increase in porosity was observed up to S_{BET} 1449 m^2 g^{-1} for UiO-66-NO_2, whereas UiO-66-NO_2/SO_3/SH exhibited an S_{BET} of *ca.* 1348 m^2 g^{-1} despite containing *ca.* 15 w/w% of functionalized modulators. The pore size distribution revealed significant differences in the microporous character of the samples. In agreement with the similar defectivity of UiO-66-SH and the pristine sample, their pore size distribution is similar. The rest of the samples have pore features of the nano-ordered ***reo*** phase.[24]

Since the modulators introduced to UiO-66 shall alter its electronic structure,[25] we applied Photoluminescence (PL) measurements to provide information about the electronic transitions, which are also related to their defective nature (Fig. S82–S91, ESI†)[23] MOFs with fewer defects, enhanced charge transfer, and more ligands will exhibit greater PL emission.[26] While the SH group is an electron donor group, the SO_3 and NO_2 groups are electron withdrawers; thus, the charge transfer between the clusters and the ligands will be different. It is important to remark that the analysis of PL in MOFs is complex due to the sensitivity of emission spectra to different factors, such as charge transfer, size, presence of defects and crystallinity among others.

A reduction in the emission intensity is observed with the addition of the –SH modulator (Fig. S82, ESI†). A more pronounced behavior occurs with the –NO_2 modulator, due to the greater decrease in the linker/metal ratio. In the case of the SO_3 modulator, only a slight reduction in intensity compared to the pristine sample is observed, as it is not only altering the electron density but also acting as a new linker.

This behaviour leads to a higher efficiency of charge transfer between the metal centres and the hemilabile Benz-SO_3 linker, consequently increasing PL emission compared to the other modulators. For samples with multiple modulators, a balance between the defects caused by the –SH and –NO_2 modulators and the improvement in charge transfer by –SO_3 is observed.

The maximum emission wavelength can also provide information about the degree of defects, as it is affected by the energy gap between the excited ligand and the metal cluster.[27] In Fig. 3a, it can be observed that the –SO_3 modulator causes a blue shift in the maximum PL emission, indicating more energetic contributions in the forbidden region of the band gap compared to the pristine sample, due to its role as a new linker, while the –NO_2 and –SH modulators cause red shifts, indicating the creation of new, less energetic energy levels

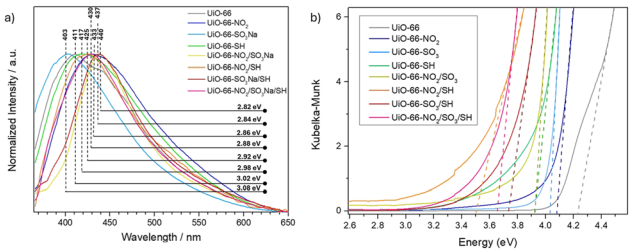

Fig. 3 (a) Normalised photoluminescence spectra of the MOFs. (b) Kubelka–Munk and tau plot of the samples to extract the bandgap.

within the forbidden region of the band gap. The emission of samples with multiple modulators all undergoes a redshift, indicating that the defects generated by the $-NO_2$ and –SH modulators outweigh the improvement in charge transfer caused by $-SO_3$. These results are supported through emission spectra deconvolutions (Fig. S83–S91, ESI†). Diffuse reflectance was applied to study the optoelectronic properties of the materials and to estimate their band gap (Fig. S92–S96, ESI† and Table 1). All MOFs showed a decrease in band gap compared to pristine UiO-66 (4.21 eV), as represented in Fig. 3b. Among the single-modulated MOFs, a smaller band gap was found for UiO-66-SH, whereas all the SH-containing multi-modulated samples have a more significant bandgap decrease, which might be affected by the higher defect induction. This result aligns with the PL findings, as adding modulators or their combination can create structural defects, altering electronic transfer processes.

All in all, the MTVM approach is proven as a versatile method for the *in situ* defect multifunctionalisation of MOFs, increasing their porosity. Introducing functional modulators alters the Zr_6 clusters of the MOF, and tunes their electronic transitions and optoelectronic properties. We anticipate that this methodology may impact the catalytic properties of MOFs among other applications.

IAL conceptualized, supervised the project, and acquired funding. CRM synthesized and characterized the materials. IAL, CRM, CCB and MA collected the PDF data. CCB treated, analysed and interpreted the PDF data. MA collected and interpreted the PL data. IAL and CMR wrote the first draft of the manuscript with input from all authors. The project that

gave rise to these results received the support of a fellowship from "la Caixa" Foundation (LCF/BQ/PR23/11980041). PDF experiments were performed at BL-04 MSPD at ALBA Synchrotron (2023087671) with the collaboration of ALBA staff. MA thanks the "Juan de la Cierva" fellowship (JDC2022-049934-I). CCB thanks Leverhulme Trust Research Project Grant (RPG-2020-005).

Data availability

Data for this article, including full characterisation, are available at Zenodo at **https://doi.org/10.5281/zenodo.12625580**.

Conflicts of interest

There are no conflicts to declare.

Notes and references

1 R. S. Forgan, *Chem. Sci.*, 2020, **11**, 4546–4562.
2 F. Bigdeli, *et al.*, *J. Mater. Chem. A*, 2023, **11**, 22105–22131.
3 I. A. Lazaro, *et al.*, *ACS Appl. Mater. Interfaces*, 2022, **14**, 21007–21017.
4 I. Abánades Lázaro, *J. Mater. Chem. A*, 2022, **10**, 10466–10473.
5 M. Taddei, *Coord. Chem. Rev.*, 2017, **343**, 1–24.
6 G. C. Shearer, *et al.*, *Chem. Mater.*, 2016, **28**, 3749–3761.
7 W. Jiang, *et al.*, *Adv. Funct. Mater.*, 2024, 2308946–2308969.
8 H. Furukawa, *et al.*, *Angew. Chem., Int. Ed.*, 2015, **54**, 3417–3430.
9 H. Deng, *et al.*, *Science*, 2010, **327**, 846–850.
10 I. Abánades Lázaro, *et al.*, *Angew. Chem., Int. Ed.*, 2020, **59**, 5211–5217.
11 M. J. Cliffe, *et al.*, *Nat. Commun.*, 2014, **5**, 4176.
12 X. Feng, *et al.*, *J. Am. Chem. Soc.*, 2020, **142**, 3174–3183.
13 L. Valenzano, *et al.*, *Chem. Mater.*, 2011, **23**, 1700–1718.
14 I. Abánades Lázaro, *Eur. J. Inorg. Chem.*, 2020, 4284–4294.
15 F. E. Chen, *et al.*, *Chem. Mater.*, 2022, **34**, 3383–3394.
16 C. Castillo-Blas, *et al.*, *Nanoscale*, 2020, **12**, 15577–15587.
17 D. A. Keen, *J. Appl. Crystallogr.*, 2001, **34**, 172–177.
18 C. L. Farrow, *et al.*, *J. Phys.: Condens. Matter*, 2007, **19**, 335219–335227.
19 H. Jiang, *et al.*, *J. Am. Chem. Soc.*, 2020, **142**, 9642–9652.
20 S. Leubner, H. Zhao, N. V. Velthoven and M. Henrion, *et al.*, *Angew. Chem., Int. Ed.*, 2019, **131**, 11111–11116.
21 F. C. N. Firth, *et al.*, *J. Am. Chem. Soc.*, 2021, **143**, 19668–19683.
22 G. Oberdörster, *et al.*, *Environ. Heal. Perspect.*, 2005, **113**, 823–839.
23 W. Morris, *et al.*, *ACS Appl. Mater. Interfaces*, 2017, **9**, 33413–33418.
24 W. Liang, *et al.*, *Dalton Trans.*, 2016, **45**, 4496–4500.
25 A. D. Vos, *et al.*, *Chem. Mater.*, 2017, **29**, 3006–3019.
26 Y. Fu, *et al.*, *RSC Adv.*, 2019, **9**, 37733–37738.
27 H. Zhu, *et al.*, *J. Lumin.*, 2019, **208**, 67–74.